Open Access

Catalysis Research

LIDSEN Publishing Inc.

Original Research

In Water High Yield and Selectivity of CH_4 and H_2 Production from CO_2 Using UVC Light and a SiO_2-surface-modified TiO_2 Photocatalysts

Oswaldo Núñez [1, 2, *], Mohammad Fereidooni [1], Victor Márquez [1], Duangthip Sattayamuk [1], Piyasan Praserthdam [1], Supareak Praserthdam [3]

1. Center of Excellence on Catalysis and Catalytic Reaction Engineering. Department of Chemical Engineering, Faculty of Engineering, Chulalongkorn University, Bangkok 10330, Thailand; E-Mails: onunez@usb.ve; fereidoonimohammad@gmail.com; marquezvictor06@gmail.com; ktnkurapicagon@gmail.com; piyasan.p@chula.ac.th
2. Laboratory of Physical Organic Chemistry and Environmental Chemistry, Department of Processes and Systems, Universidad Simón Bolívar (USB), Caracas 1080A, Venezuela
3. Performance Computing Unit (CECC-HCU), Center of Excellence on Catalysis and Catalytic Reaction Engineering (CECC), Chulalongkorn University, Bangkok 10330, Thailand; E-Mail: supareak.p@chula.ac.th

* **Correspondence:** Oswaldo Núñez; E-Mail: onunez@usb.ve

Academic Editor: Anna Zielińska-Jurek

Special Issue: Green Photocatalysis for Degradation of Emerging Contaminants and Hydrogen Production

Catalysis Research
2023, volume 3, issue 4
doi:10.21926/cr.2304029

Received: August 25, 2023
Accepted: November 28, 2023
Published: December 05, 2023

Abstract

To improve CH_4 and H_2 formation from CO_2 photoreduction using non-organic, non-laborious, and inexpensive photocatalysts, we have prepared two surface-silicate-modified TiO_2 catalysts: P25-SiO_2 and AmTiO_2-SiO_2 (amorphous TiO_2) to be tested in water and using UV light. The last catalyst produces more CH_4 and H_2 in water than P25 (3:1 TiO_2 anatase: rutile) under UV light irradiation of HCO_3^- and CO_2; am-TiO_2-SiO_2 at pH = 7, produces 8 times more CH_4 and H_2 than P25 with selectivity at the reactor headspace of 30% and 53%, respectively. Using CO_2 (pH = 3), 80 times more CH_4 than P25 under the same conditions is

obtained with a yield of 71%. This corresponds to a production of 8.9 µmol $g_{cat}^{-1}\cdot h^{-1}$, one of the highest reported rates of CH_4 production from CO_2 using carbon-free semiconductors. H_2 is also produced by water splitting using Am-TiO_2-SiO_2 and water at low pH. The enhanced reactivity compared to P25 is attributed to three main factors: a) Low catalyst PZC (4.1) that facilitates CO_2 adsorption and proton availability at the active site to catalyze the e transfer from Ti at the TiO_2-SiO_2-carbonate adduct b) SiO_2 acts as electron trap reducing carriers recombination (External intramolecular trapping (EIT) mechanism) and c) am-TiO_2-SiO_2, light collection efficiency, surface area and irregular atoms distribution. Catalysts were also tested for Methylene blue (MB) photooxidation. P25 is quite a better catalyst in oxidizing MB via OH radicals, probably due to the more positive valence band potentials in the SiO_2-modified catalysts that avoid the OH radical formation from water; however, when bicarbonate is added to MB solution, am-TiO_2-SiO_2 catalysts reactivity increases as a consequence of its valence band down-bending.

Keywords

Amorphous TiO_2-SiO_2; CO_2/HCO_3^- photoreduction; H_2 and CH_4 selectivity; electron traps; cyclic voltamnetry; open circuit potential decay; point of zero charge; OH radical formation inhibition

1. Introduction

Production of methane and hydrogen through CO_2 photoreduction is of great interest not only from the environmental point of view but also due to the generation of combustible gases that can be converted into value-added products such as Methanol. The last conversion could be achieved via thermo-catalysis with a low performance/price ratio. However, this conversion can be performed via photo-catalytic oxidation of low-concentration methane over decorated graphitic carbon nitride [1, 2]. H_2 and CH_4 are sources of energy storage that can also be produced from CO_2. As suggested, co-mixing H_2 and CH_4 may double the energy storage capacity compared with pure hydrogen or methane storage [3]. Therefore, more energy can be obtained by storing the gases produced by CO_2 photo reduction with UV/solar light. CO_2 may then be considered as a feedstock. Large surface areas of 2D materials and conjugated microporous polymers (CMPs) allow the storage of combustibles such as H_2 and CH_4 and their energy storage conversion [4, 5].

In water, CO_2 photo reduction conversion to CH_3OH, HCOOH, and CH_3COOH using visible light and 2D/2D zinc vanadium oxide-reduced graphene oxide (ZnV_2O_6/RGO) nanosheets has been recently reported; up to 5154 µmolg_{cat}^{-1} of CH_3OH is produced [6]. This efficiency is attributed to the trapping and transporting of electrons by reduced graphene oxide (RGO). Also, 3488 µmolg_{cat}^{-1} CH_3OH production has been obtained using ZnV_2O_6/RGO/g-C_3N_4 composite [7].

Reports on CH_4 and CO production of 225 µmol$g_{cat}^{-1}h^{-1}$ from CO_2 UV-photo reduction using MXene/Clay (2D/2D/2D O-C_3N_4/Bt/$Ti_3C_2T_x$) composite and up to 145 and 133 µmolg_{cat}^{-1} h^{-1} with WO_3/g-C_3N_4 and visible light represent quite high yields results [8, 9]. CO_2 photoreduction using pg/C3N4/Ti_3AlC_3/TiO_2 composite has been reported to yield 91.9 and 4.97 mmol$g_{cat}^{-1}h^{-1}$ [10]. MXene based cocatalyst: TiO_2A/Ti_3C_2/TiO_2R MXene yield85 and 18 mmol$g_{cat}^{-1}h^{-1}$ of CO and CH_4,

respectively [11]. S-scheme has been proposed for producing 2103.5 $\mu molg_{cat}^{-1}h^{-1}$ of CH_4 with 96.59% selectivity using g-C_3N_4/TiO_2/$TiAlC_2$2D/OD/2D composite [12]. However, results using carbon-based semiconductors as g-C_3N_4 to generate CH_4 from CO_2 must be carefully interpreted since some CH_4 formed may be produced by the reduction of carbon source in the catalyst. Therefore, control experiments without CO_2 must be conducted to verify the non-formation of Methane or Methanol under these conditions [13-15]. Other studies reported isotopic labeling (^{13}C and ^{18}O) to evaluate carbon and oxygen sources unequivocally [16-19].

Non-carbon-based photocatalysts such as $ZnFe_2O_4$/Ag/TiO_2 nanorods have been successfully used to produce CO, CH_4 and CH_3OH via UV/visible photo reduction of CO_2 [20]; up to 1566 $\mu molg_{cat}^{-1}$ CO yield has been obtained using 3D MAX Ti_3AlC_2/TiO_2 in a monolith photo reactor where efficient formation of CH_4 via reforming is also reported [21].

SiO_2-TiO_2 materials are used in very different fields [22]. As a photocatalyst, CO_2 photo reduction enhancements have been reported. However, in the cases said TiO_2 is either embedded in SiO_2 matrices or anchored on glass [23, 24]. In fact, in these cases, photoredox reactions are faster than TiO_2 since the band gap is relatively larger (up to 4.11 eV) than the TiO_2 one (3.2 eV); therefore, the CB (Conduction band) reduction and VB (Valence Band) oxidation potentials increase. Nevertheless, SiO_2 coating TiO_2 P25 has also been used to reduce CO_2 to CO. Only CO and H_2 were detected, and CO selectivity increased compared to unmodified P25 [25]. Toluene degradation using novel mesoporous SiO_2-doped TiO_2 nanofibers has been reported [26]. Zirconium-doped TiO_2/SiO_2 and visible light have been used to degrade VOC, including Toluene [27]. Simulated-sunlight-activated photocatalysis of Methylene Blue (MB) using cerium-doped SiO_2/TiO_2 nanostructured fibers has also been reported [28].

Crystalline TiO_2 modified with tailored nanostructures has been extensively studied [29]; however, many properties associated with semiconductors' atom arrangements influence their photocatalytic activity. Therefore, using amorphous TiO_2 (am-TiO_2) may bring essential advantages due to the porosity (high specific area), its high light-harvesting capacity, and the atom disorder that might induce charge separation. C-doped am-TiO_2 has been synthesized and used in the photo reduction of CO_2, obtaining CH_4 production of 4.1 $\mu molg_{cat}^{-1}h^{-1}$ [30]; this catalyst showed a high specific surface area and narrowed band gap of 2.1 eV. Additionally, it has been pointed out that introducing oxygen vacancies on the C-doped am-TiO_2 can efficiently accelerate charge separation and transportation of photo-generated hole-electron pairs, enhancing photocatalytic performance [31]. However, am-TiO_2 has been investigated less than its crystalline forms, applications that do not require high temperatures have been reported. For instance, its antibacterial capacity has been studied [32]. Density-functional theory (DFT) calculations of structural and electronic properties of am-TiO_2 as a photocatalyst for hydrogen production have been published [33]. Mesostructured SiO_2-TiO_2 mixed oxides with enhanced stability, textural properties, and surface area in the 290-346 m^2/g range have been synthesized [34].

We have identified some relevant aspects that may help to increase the CH_4 formation rate from HCO_3^-/CO_2 UV light photo reduction [35]. For instance, CO_2/HCO_3^- adsorption and the corresponding adduct concentration increases at pH equal and above P25 point of zero charge (PZC = 6.2) [36]; however, electron transfer from Ti to form the radical anion Ti^{+4}-OCO_2^- requires protonation, that is also needed to produce H_2 via water splitting. Therefore, a TiO_2 surface modification must be oriented to increase the negative charge on the surface, but at the same time, more protonation capacity than TiO_2 at the catalyst surface is required. CO formation

contribution from the oxygen vacancy (Vo) sites must also be minimized to increase CH_4 formation during the photocatalytic reaction.

To fulfill the three previous aspects, we have modified am-TiO_2 by attaching SiO_2 to its surface at room temperature and pressure. Since SiOH is a more vital Bronsted acid than TiOH, PZC of the SiOH at the surface-modified TiO_2 must be lower than unmodified TiO_2; therefore, at neutral pH, the catalyst surface must be negatively charged, which may improve CO_2 adsorption and its photoreduction rate; furthermore, to orient the photoreduction to more CH_4 and H_2 formation, the proton must also be available (SiOH) at the catalyst active site; therefore, using this surface-SiO_2 modified TiO_2 catalyst, CH_4 formation rate is expected to improve as compared to unmodified TiO_2 at neutral pH. Further rate improvement is likely when pH changes to the new motivation PZC value. The amorphous condition of the synthesized catalyst may also improve the CO_2 photoreduction rate due to increased surface area, light harvesting, and decreased e/h recombination.

In this work, amorphous TiO_2 was synthesized via the sol-gel method, and its surface was modified by its addition to a tetraethyl orthosilicate acid solution. Complete characterization of the solid product obtained is reported. It includes SEM-EDX, TEM, DRS, FT-IR, BET, XPS, XRD, PZC measurement, and Raman spectroscopy. Additionally, catalyst (supported on ITO) current density, de-trapping capacity, surface potential, and electron transfer processes to the electrolyte are also reported using cyclic voltammetry (CV) and open circuit potential decay (OCPD) measurements.

Our approach is to introduce modifications of catalysts without using organic compound additives and as simple as possible to increase CH_4 and H_2 production and reduce the cost of catalyst preparation. Herein, we report essential CH_4 and H_2 production improvement from CO_2/HCO_3^- using silicate surface modified amorphous TiO_2 and UVC (200-280 nm) light. A necessary amount of H_2 is also produced from water splitting. Some insights on the reaction mechanism obtained using electrochemistry and photooxidation measurements are also reported, pointing to the role of the (d-p) π-bonding at the Si-O bond and the non-formation of hydroxyl radical at the catalyst valence band.

2. Materials and Methods

2.1 Materials

The following chemicals and solvents were used: Degussa (P25, Aeoxide); sodium hydroxide (NaOH, 99.0%, Emsure); hydrochloric acid (HCl, 37%, Ensure); sodium phosphate monobasic dehydrate ($NaH_2PO_4{\cdot}2H_2O$, 99.0%, Acros Organics); sodium hydrogen carbonate ($NaHCO_3$, 99.0%, Fluka Chemika); acetic acid (CH_3COOH, 100%, Merck); titanium (IV) tetraisopropoxide ($Ti[OCH(CH_3)_2]_4$, 98%, Aldrich); tetraethyl orthosilicate ($Si(OC_2H_5)_4$, 98%, Aldrich); methylene blue (Sigma-Aldrich); Ethyl Alcohol (C_2H_6O, 99.9% QRëC) and water (H_2O, 17.7 MΩ/cm, Nanopure). The following gases were used: methane (CH_4, 99.99%, Linde); hydrogen (H_2); carbon monoxide (CO, 99.99%, Boc Gases); carbon dioxide (CO_2, 99.99%, Linde); helium (He, >99.99%, Linde); argon (Ar, >99.99%, Linde); nitrogen (N_2, >99.99%, Linde); air (>99.99%, Bangkok Industrial Gas).

2.2 Characterization, Photo Reduction, and Gasses Concentration Measurements

Semiconductor morphologies and crystalline structures were obtained by Scanning electron microscopy and energy-dispersive X-ray Spectroscopy (SEM-EDX). An Amicus photoelectron spectrometer with an Mg Kα X-ray source (20 mA and 10 keV) controlled by Kratos Vision2 software. C 1 s peak at 284.6 eV was used for calibration. Using a Lamda 650 UV/Vis instrument. A JEOL JEM-2100 Electron Microscope was used to obtain the Transmission Electron Microscope (TEM) images. Diffuse Reflectance UV-Vis Spectra (DRS) was collected using UV Win Lab software from PerkinElmer. Using Tauc's equation, $(\alpha h\nu)^{1/n} = A(h\nu - Eg)$, the semiconductors band gap (Eg) was obtained. In the last equation, α is the absorption coefficient, h is Planck's constant, ν and λ, light frequency and wavelength, A is an optical constant, and n = 0.5 for direct transitions. FT-IR Reflectance Spectroscopy (FT-IR) spectra were obtained in a Nicolet 6700 FT-IR instrument. A Horiba 4P-Fluoromax spectrofluorometer with a Xenon lamp (200-800 nm) was used to obtain the corresponding Photoluminescence (PL) spectra. The specific surface area of the catalysts was estimated by the Brunauer-Emmett-Teller (BET) method using a model Asap 2020, Micrometrics instrument. The point of zero charge (PZC) was obtained by plotting a solid catalyst pHi-pHf Vs in water. pH_i where pH_i and pHf are initial and final-equilibrium pHs; a Metter Toledo Seven multi pH-meter was used. Surface quantitative analysis was obtained using X-ray Photoelectron Spectroscopy (XPS) using an Amicus spectrometer at a voltage of 15 kV and current of 12 mA with Mg Kα X-ray radiation (1253.6 eV) and Al Kα X-ray radiation (1486.6 eV). Crystal structures were determined by X-ray Diffraction (XRD) using a Bruker D8 Advance instrument using a data collection ($0.05°s^{-1}$) at a 20°-80° angle range. The crystallite size was calculated using the Debye-Scherrer equation. Raman spectra were obtained using a Horiba Scientific LabSpec 6 instrument.

Photoreduction was performed in a cylindrical quartz reactor surrounded by six 16-watt Philips Germicidal Ozone UVC (200-280 nm) bulbs. A Shimadzu GC-14A instrument was used to quantify CH_4 reactor headspace with a FID detector provided with a Shincarbon ST packed column at 70°C in 10 min of analysis and using He as carrier gas and air as make-up gas with injector and detector temperatures of 150°C. H_2 and CO were measured using a Shimadzu GC-8A instrument with a TCD detector and molecular sieve 5A column at 70°C for 18 min. Ar was used as carrier gas with injector and detector temperatures of 150°C.

2.3 Synthesis

2.3.1 Amorphous TiO_2 (Am-TiO_2)

Following the sol-gel method, 5 mL of acetic acid in 50 mL of Ethanol (95%) solution previously stirred for 30 min and 6.3 mL (0.021 mol) of titanium tetraisopropoxide were added dropwise while stirring for 15 min. Stirring was continued for one hour [31]. 10 ml of the above mixture was left to dry in the air at room temperature. White powder of TiO_2 was collected and used directly to obtain am-TiO_2-SiO_2.

2.3.2 Silicate-Surface Modified TiO_2 Catalysts (am-TiO_2-SiO_2)

While stirring to a solution of 35 ml of Ethanol and 35 ml of distilled water, microliters of HCl solution (35%) were added until pH = 3 was reached. Then, (5 mmol) of tetraethyl ortho silicate

was added to the solution. Stirring was continued for 6 h. 2 g of catalyst (P25 or am-TiO_2) was added to the final mixture; stirring continued for 1 h. The solution was dried at room temperature for 24 h. Catalyst-SiO_2 was air-dried at 110°C for 15 min.

2.3.3 Reuse am-TiO_2-SiO_2

Catalysts am-TiO_2-SiO_2 used for CO_2 photo reduction (pH = 3) were removed from the reactor, and the water-catalyst mix evaporated at 90°C until the dry catalyst was obtained (0.2 g). The 0.3 g of catalyst needed for the reaction was completed with the catalyst used at pH = 7. The obtained powder was used directly as a reused catalyst for CO_2 photoreduction.

2.3.4 Catalysts Supported on ITO

The ITO (Indium Tin Oxide) electrodes were treated with a KOH 0.05% solution and rotated at 1000 RPM to remove the excess of the critical two times before the catalysts' coating. A suspension of P25-SiO_2 catalyst in ethanol was prepared using 20 g of catalysts and 20 mL of ethanol and sonicated for 3 minutes (6 rounds, 30 s each time). am-TiO_2-SiO_2 gel was directly added to ITO. The ITO Electrodes were entirely covered with the suspension/gel and rotated at 1000 RPM to remove the excess material. The covered electrodes were air-dried and then treated at 150°C for 10 minutes. The Catalysts supported on ITO were stored in a closed flask for later use.

2.4 CO_2/HCO_3^- Photo Reduction

A 250 mL three-way cylindrical quartz reactor provided with a sand sparger for bubbling gas into the solution was used. Into this flask, a solution of $[CO_2]_w$ = 34 mmol/100 mL by bubbling CO_2 on 100 mL of water or $[HCO_3^-]$ = 2.3 mmol/100 mL and 0.3 g silicate surface-modified TiO_2 catalyst was added. pH (3-8) was adjusted using HCl, NaOH or 100 mg/L of NaH_2PO_4 buffer solutions. The reaction was started by turning on the light while stirring. Irradiation was continued for 4 hours. The reactor temperature was maintained at 30°C. The resultant reactor headspace gas samples were taken every 0.5 hours using a 2.5 ml gas syringe (injecting 0.5 mL) and analyzed using GC-FID and GC-TCD. CH_4, CO, and H_2 calibration curves were used to obtain their concentration during the kinetic runs [36]. Figure S1 shows the reactor setup for CO_2 photo reduction, and Figure S2 is a $[CH_4]$ calculation example.

2.5 Electrochemical Experiments

All experiments were performed using an Autolab® potentiostat/galvanostat M240, a Metrohm® Ag/$AgCl_{(sat)}$ reference electrode, a Platinized Titanium mesh as the counter electrode, and the catalysts supported on ITO as working electrodes. The solutions were prepared using Deionized Water (DI) (18 MΩ/cm^2) and pH adjusted to 7 using a 0.1 M Na_2HPO_4/NaH_2PO_4 Buffer solution. Experiments were performed in a conventional three-electrode single-chamber cell. The solution was purged with high-purity nitrogen for 30 min before the measures. The concentration of $NaHCO_3$ used was 0.1 M. To measure Semiconductors´ Open Circuit Potential Decay (OCPD), a 0.8 V potential was applied for 20 s until the current stabilized. After that, the circuit was opened and the working electrode's potential was followed for 10 minutes [37]. To obtain Cyclic Voltammetry (CV) graphs, a scan rate of 10 mV/s was used [38].

2.6 Methylene Blue Photooxidation

Methylene blue (MB) Absorption Vs. a concentration calibration curve (Abs = 0.184 [MB] + 0.0047; R^2 = 0.998, at 664 nm) of 4, 2, 1, and 0.5 mg/L were used to follow MB photooxidation using am-TiO_2-SiO_2 and P25 catalysts.

In each batch, 5 mg of the catalyst was dispersed in 100 ml of 8 ppm MB solution. Before photo-irradiation, the suspension was stirred for 30 min in the dark to reach adsorption/desorption equilibrium. Samples were taken at different time intervals during the photocatalytic reaction, and the catalyst was immediately separated from the solution by a syringe filter. UV-vis spectra was taken, and MB degradation followed at 664 nm. Photodegradation pseudo-first-order rate constants were obtained from plots of ln [MB] Vs. Time. Exponential [MB]/[MB]o Vs. t plots and % photodegradation = ([MB]o - [MB]t)/[MB]o x 100 Vs. t was also obtained. pH was measured at the beginning and the end of each kinetic run.

3. Results and Discussion

3.1 Catalysts Characterization

Figures 1a and 1b show absorption spectra (DRS) and band gaps (Eg) of the synthesized silicate-surface modified catalysts obtained according to Tauc's equation. These band gaps are equal to or lower than the corresponding P25 one (3.20 eV). For instance, the P25-SiO_2 band gap does not change compared to P25. However, amTiO_2-SiO_2 moves down to 3.13 eV (396 nm). This value, together with the Cu-TiO_2-SiO_2 one (3.06 eV, 405 nm), is in the violet visible region. Therefore, visible light-photo reduction activity is expected for these catalysts. Cu-P25-SiO_2 and N-P25-SiO_2 have been previously synthesized in our laboratory, and their band gaps are included just for comparison.

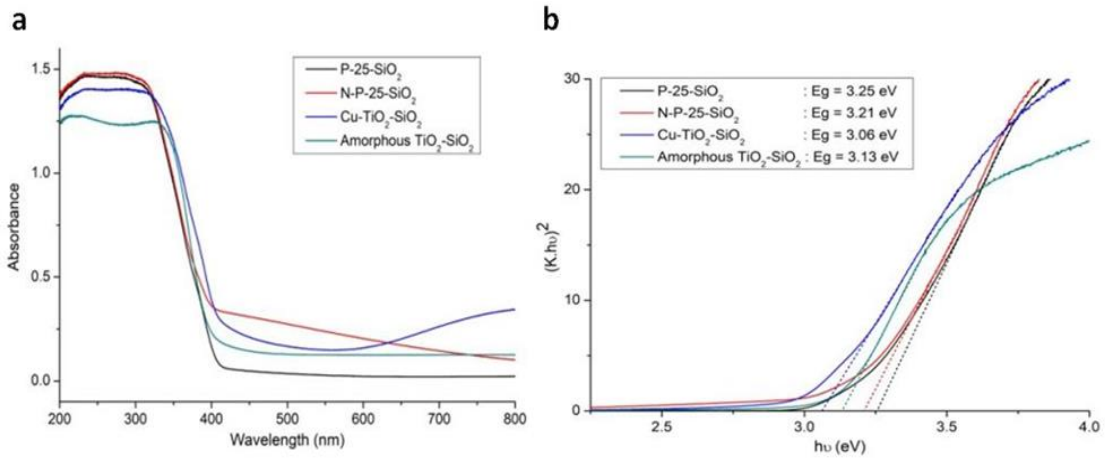

Figure 1 a Absorption spectra and **b** Plots of $(K.hv)^2$ vs. hv according to Tauc's equation: (αhv)1/n = A(hv-Eg), n = 0.5. Obtained band gaps of P25-SiO_2 and am-TiO_2-SiO_2, are shown. Band gaps are also shown for comparison previously synthesized in our laboratory N-P25-SiO_2 and Cu-P25-SiO_2.

In Table 1, characterization parameters of SiO_2-surface modified TiO_2 catalysts are shown. am-TiO_2-SiO_2 and P25-SiO_2 catalysts show larger surfaces than P25. These differences may contribute

to improving these catalysts´ photo-reduction performances. Table S1 shows BET results between am-TiO_2 and am-TiO_2-SiO_2. The last catalyst shows a larger surface area, pore size, and pore volume than the unmodified am-TiO_2 one. The following characteristic IR signals were observed for the two silicate-surface-modified catalysts: 670 cm^{-1}, Ti-O-Ti asymmetric stretching; 1060 cm^{-1}, Si-O-Si symmetric stretching; 960 cm^{-1} Si-O-Ti stretching; 3750 cm^{-1}, SiO-H extending and a broadband 3700-3500 cm^{-1} corresponding to water adsorbed on catalysts. These signals have also been identified in SiO_2-TiO_2 hybrid spheres and sol-gel TiO_2-SiO_2 films [39, 40]. FT IR spectrum of am-P25, am-P25-SiO_2, am-TiO_2, and am-TiO_2-SiO_2 are shown in Figure S3. O-Si-O stretching signal at 1022-1080 cm^{-1} is present only in the -SiO_2-modified catalysts.

Table 1 Catalysts band gap (Eg), EDX-SEM weight percentage (Wt %), surface area, pore size/volume, and IR signals.

Catalyst	band gap Eg (eV)	Wt (%)	Surface Area[a] (m^2/g)	Pore size a (Å) Pore volumen[a] (cm^3/g)	IR (cm^{-1})
P25-SiO_2	3.08	Ti: 48.00; Si: 3.21; O: 48.79	141.13 m^2/g	62.63 0.22	670 960 1060 3750 3700-3500
am-TiO_2-SiO_2	3.05	Ti: 53.77; Si:5.13; O: 41.10	264.37 m^2/g	24.55 0.16	

[a]P25: 45.7-54 m^2/g and 0.177 cm^3/g.

Figure 2a and Figure 2b show photoluminescence spectra of am-TiO_2-SiO_2 and P25-SiO_2 catalysts using exciting light at 350 and 250 nm, respectively. More light collection efficiency is shown for am-TiO_2-SiO_2, especially when exciting light of more energy (UV at 250 nm) is used. It can be ascribed to the removal of electron capture centers on the surface of am-TiO_2 or the removal of nonradiative decay channels due to the SiO_2 shell around am-TiO_2 [41]. This light harvesting efficiency may improve this catalyst photo activity. Figure 2c shows SEM-EDX results of am-TiO_2-SiO_2. Agglomerations of irregular particle sizes and homogeneous Si and O distribution (EDX) at the catalyst surface spot are observed. TEM images of am-TiO_2-SiO_2 and P25-SiO_2 are shown in Figure S4. Agglomerations and amorphous morphology are detected for amTiO_2-SiO_2. Meanwhile, crystalline morphology for P25-SiO_2 is revealed. According to EDX, prepared am-TiO_2-SiO_2 contains an average of 53% Ti, 5% Si, and 41% O wt% at the surface. We will use the active site of this surface structure to depict the catalytic aspects covered in this work. Figure 2d shows a PZC value of 4.1 for am-TiO_2-SiO_2 obtained from pH_i-pH_f Vs—pH_i plot.

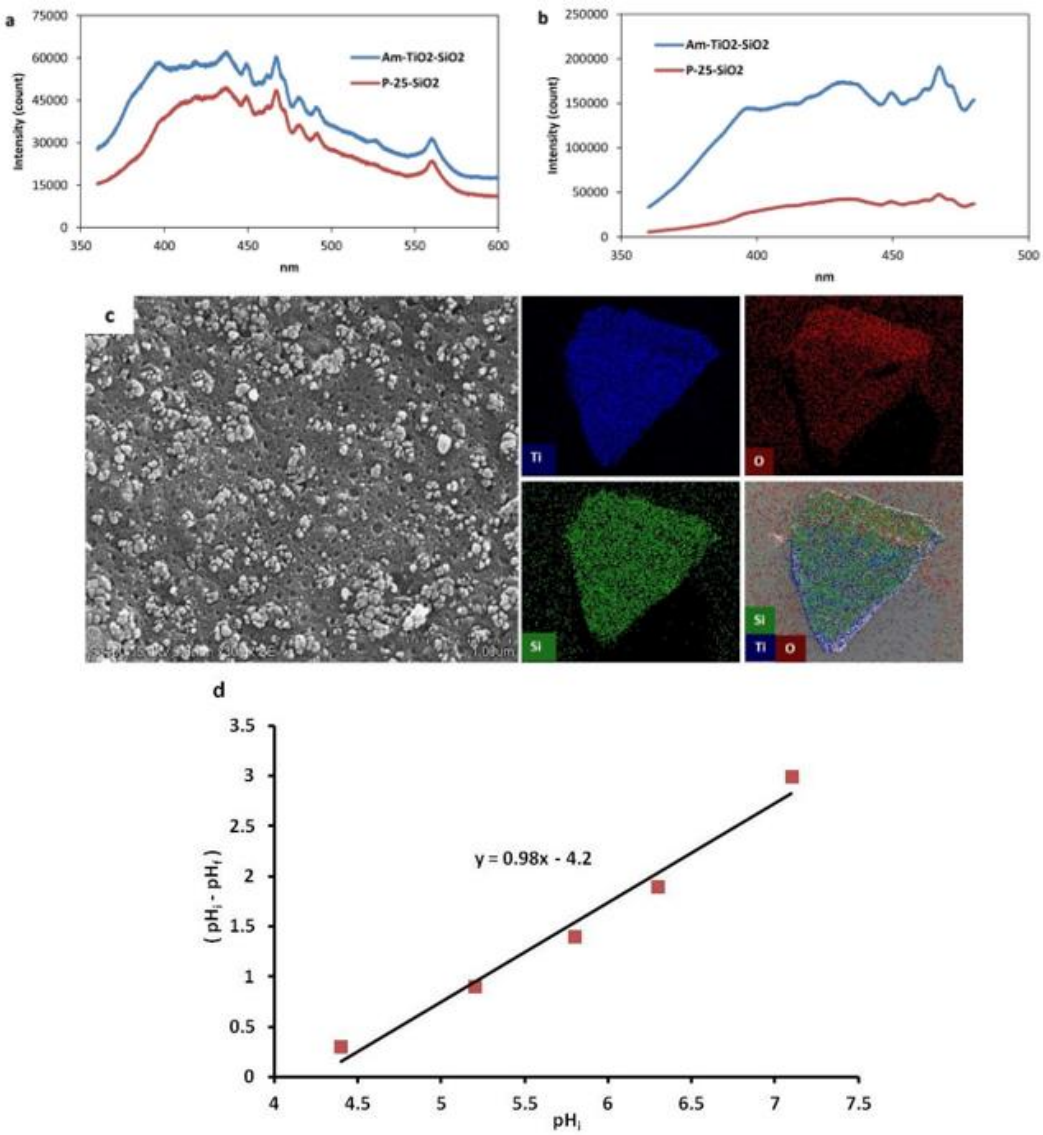

Figure 2 a 320 nm excitation photoluminescence spectra of am-TiO_2-SiO_2 and P25-TiO_2 catalysts. **b** 250 nm excitation. **c** SEM-EDX of am-TiO_2-SiO_2. **d** am-TiO_2-SiO_2 PZC measurement.

The oxidation state of the constituent elements in the synthesized catalysts was determined using X-ray photoelectron spectroscopy (XPS), and the results are presented in Figures 3a, 3b, and 3c. The XPS spectrum of Ti 2p in Figure 3a was deconvoluted into two peaks with binding energies of 458 eV and 463.7 eV, attributed to Ti 2p3/2 and Ti 2p1/2, respectively. This confirms an oxidation state of +4 for Ti. Additionally, the Si 2p spectrum (Figure 3b) peaked at a binding energy of 102.2 eV, which was attributed to the Si-O-Ti bond. Furthermore, in the O 1 s XPS spectrum (Figure 3c), three deconvoluted peaks located at 529.8 eV, 530.9 eV, and 532 eV were attributed to Ti-O, Si-O-Ti, and surface hydroxyl groups, respectively.

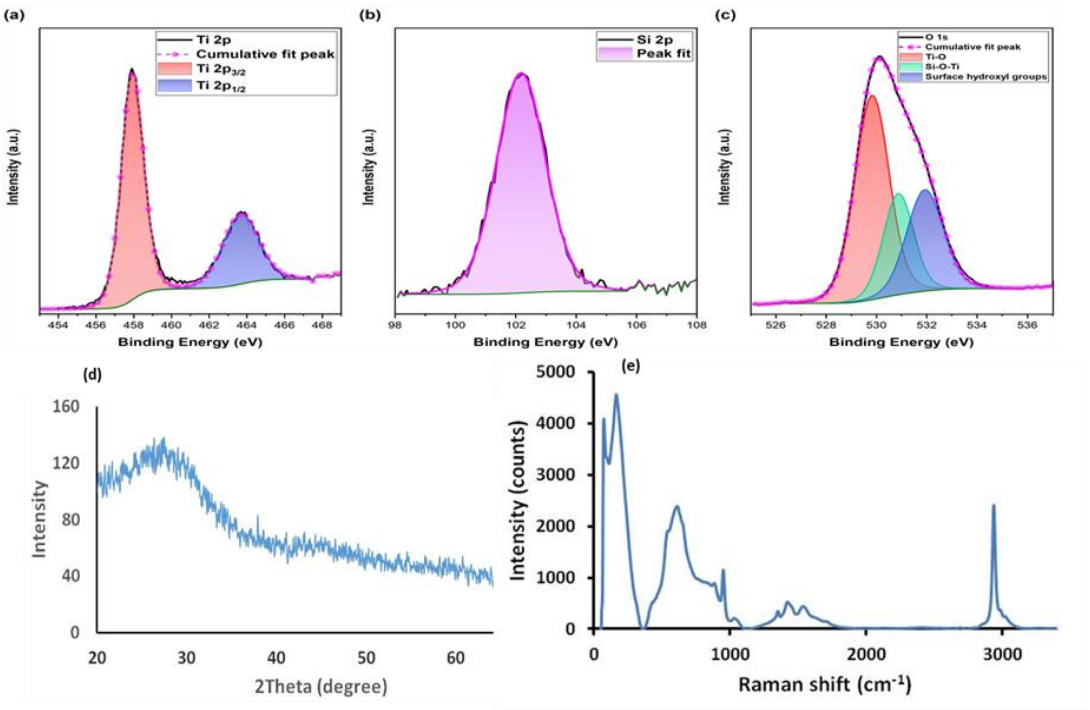

Figure 3 Ti (a), Si (b), and O (c) XPS spectra of am-TiO_2-SiO_2. (d): XRD spectrum. (e) Raman spectrum.

In Figure 3d, the XRD spectrum of am-SiO_2-TiO_2 is shown. Only one broad signal at ca. 27.5 2θ is observed. This signal is typical of amorphous TiO_2, where no crystal TiO_2 patterns are observed. Due to the small amounts of Si (5%) present, the corresponding signal at ca. 58 2θ is barely detected in Figure 3d [40].

Figure 3e shows a sharp signal at ca. 3000 cm^{-1} Raman shift corresponding to O-H stretching. This band is hidden in the corresponding FTIR due to the presence of water. Broad movements centered at 1400, 700, and 170 cm^{-1} Raman shifts can be identified as titanium species' framework [42]. A signal at 80 cm^{-1} Raman shift observed in Figure 3e could be assigned to the framework of Si since it is absent in the am-TiO_2 Raman spectrum (Figure S5).

3.2 Blanks and Alternative Carbon Sources

As shown in Figure 4, CH_4 is formed even without adding any CO_2 source (CO_2 or $NaHCO_3$). This alternative source could come from the catalyst synthesis or reactor walls' remaining organic materials. Special care is taken to eliminate any solvent from the catalyst by heating the solid catalyst while stirring at 80°C for 24 h before use. Likewise, the glass reactor is cleaned after use using successive 30 min washing of ultrasound (H_2O), KOH (EtOH), H_2SO_4 (H_2O_2), and HCl (30%). The maximum CH_4 observed after 1 h is ca. 0.5 nmol/mL H_2O g_{cat}. As observed in Figure 4, the contribution of this source is relatively low compared to the amount of CH_4 produced from CO_2 reduction. Using a new reactor, blanks with catalyst, CO_2 source, and lamp off and without catalysis, CO_2 source and lamp on were run. Under these conditions, [CH_4] < 0.05 nmol/mL H_2O g_{cat} was detected.

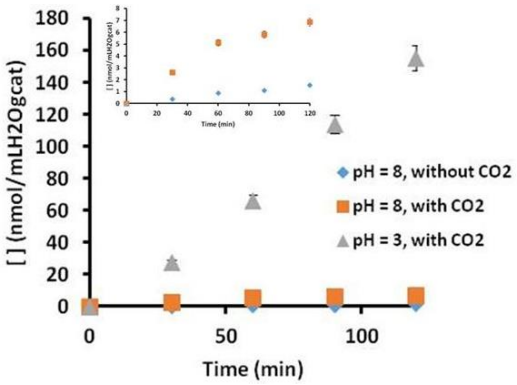

Figure 4 CH_4 photoreduction formation without and with CO_2 source at two different pHs.

3.3 HCO_3^-/CO_2 Photoreduction

P25 CO_2/HCO_3^- photo reduction proposed mechanism to form CH_4, CO, and H_2 in the reactor headspace consists of a fast formation of monodentate adduct followed by a rate-limiting adduct radical anion formation [35]. Since the Point of zero charge (PZC) of the silicate surface modified TiO_2 catalysts a ca. 2.9 [43] and 4.1 (Figure 2d) for the am-SiO_2-TiO_2 synthesized in this work, relatively lower values than the PZC (6.2) of P25, negative charge at the silicate surface must be present even at acid pH. Since a negative charge on one of the oxygen (-Si-O^-) remains, adduct formation is favored when carbonate or CO_2 is present (Scheme 1, center-top). Nevertheless, one -Si-OH is still prorogated at pH ca. 5; therefore, the proton required in the e^-transfer from Ti to produce the corresponding radical anion (Scheme 1, left-bottom) is available at the active site. Since this transfer has been pointed out as the photo reduction rate-determining step (rds), faster product formation may be observed when these silicate-surface-modified TiO_2 catalysts are used [35].

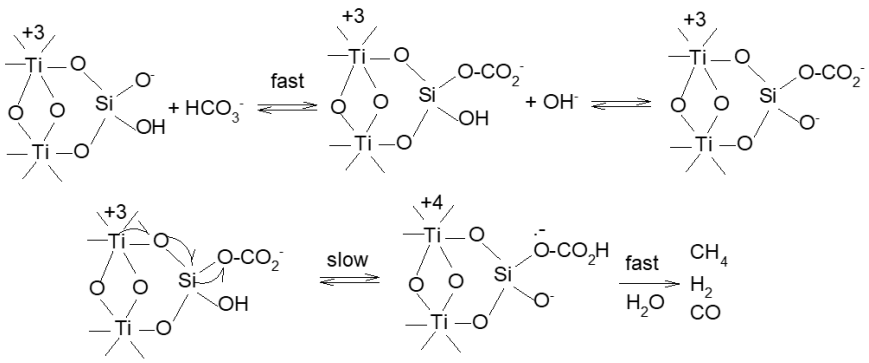

Scheme 1 TiO_2-SiO_2 carbonate adduct formation and electron transfer to form the corresponding adduct radical anion followed by fast product formation.

Figure 5a and Figure 5b show CH_4 and H_2 production in the photo reduction of HCO_3^- using the silicate-surface modified TiO_2 catalysts synthesized in this work. As expected, am-TiO_2-SiO_2 is the best catalyst, producing ca. 8 times more methane and H_2 than P25 in a non-buffered solution. Given this result in H_2 production, we performed water splitting using am-TiO_2-SiO_2 (Figure 5c). As shown in the figure, H_2 is formed with a rate of 2.3 nmol/mL_{H2O}·g_{cat}·h, that is 0.23 µmol/g_{cat}·h. This

means that am-TiO_2-SiO_2 can also be used by adding water at pH = 3 to obtain H_2 at a relatively reasonable rate. Scheme 2 shows the proposed mechanism for water splitting and H_2 formation when the carbonate adduct is present at the catalyst surface.

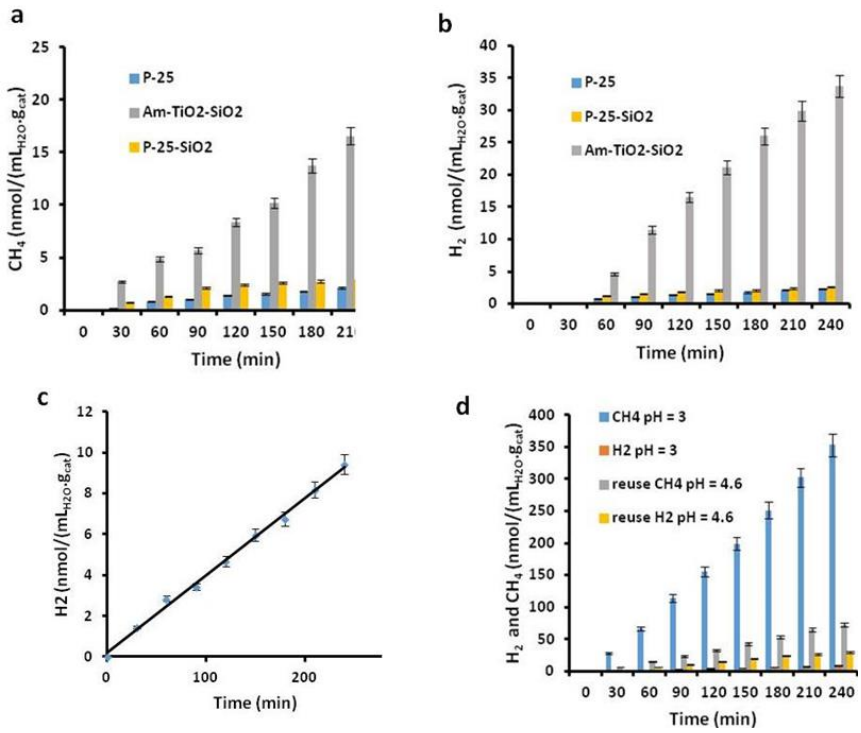

Figure 5 a reactor headspace [CH_4] produced in water UV photo reduction of 100 mg of $NaHCO_3$ using 0.3 g of catalyst under non-buffered conditions. **b** [H_2] production. See Table 2 for the reaction's initial pH values. **c** [H_2] formation rate via water splitting, without any carbonate source added at pH = 3. **d** Reactor headspace [CH_4] and [H_2] produced in water UV photo reduction of 3.4 mmole/100 mL of CO_2 using 0.3 g of am-TiO_2-SiO_2 catalyst at pH = 3. Re-used catalysts results ([CH_4] and [H_2]) at pH = 4.6 are also shown.

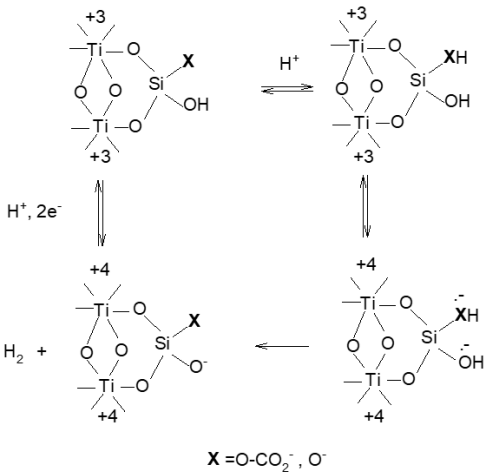

Scheme 2 H_2 production proposed mechanism for am-TiO_2-SiO_2. With CO_2/HCO_3^- added (X = O - CO_2^-) and without carbonate source added (X = O) (water splitting).

Table 2 Production and yield of CH_4 and H_2 in the HCO_3^-/CO_2 photo reduction using am- TiO_2-SiO_2. P25 is included as a reference.

Catalyst	pH	$[NaHCO_3^-]_o$ = 2.3 mmol/100 mLH_2O **CH_4 H_2** ($\mu mol g_{cat}^{-1}h^{-1}$) Selectivity % ( ) Error < 5%		pH	$[CO_2]_o$ = 3.4 mmol/100 mLH_2O **CH_4 H_2** ($\mu mol g_{cat}^{-1}h^{-1}$) Selectivity % ( ) Error < 5%		H_2O 0.3 g of catalyst **H_2** $\mu mol g_{cat}^{-1}h^{-1}$ Error < 5%
P25	9	0.06[a]	0.11[a]	4.5	0.16[a]	0.36[a]	[b]
P25-SiO_2	8.8	0.07	0.06	[b]	[b]	[b]	[b]
am-TiO_2-SiO_2	8	0.48(30)[c]	0.84 (53)	3	8.9 (71)	0.20 (2)	0.24
am-TiO_2-SiO_2 1rst reuse	[b]	[b]	[b]	4.6	1.8 (63)	0.75 (26)	[b]
am-TiO_2-SiO_2	8.4	0.12 (11)	0.41 (40)				
am-TiO_2-SiO_2	6.3	0.35 (43)	0.17 (21)	[b]	[b]	[b]	[b]
am-TiO_2-SiO_2	5	5 (98)	0.1 (2)				
am-TiO_2-SiO_2	6.3 (NaH_2PO_4)	0.35 (79)	0.09 (21)	[b]	[b]	[b]	[b]
am-TiO_2-SiO_2	5.3 (NaH_2PO_4)	0.55 (70)	0.24 (30)	[b]	[b]	[b]	[b]

[a] These values correspond to 4 h irradiation (240 min in **Figure 5** and **Figure 6**) and were obtained by dividing by 40 (100 mL/(1000 nmol/µmol. 4 h)) the values in figures. [b] No experiment was performed under this condition. [c] CO% = 100% - (CH_4 + H_2)%.

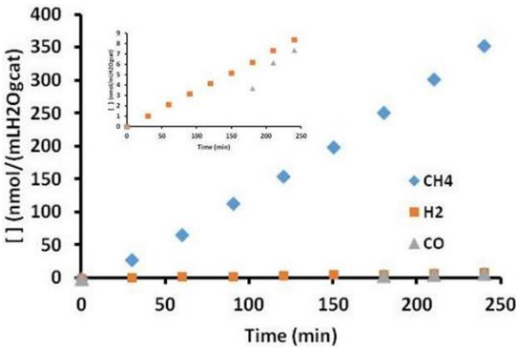

Figure 6 CH_4, H_2, and CO produced in the photocatalyzed UV reduction of CO_2 at pH = 3.

Since the reactor $[CO_2]_w$ = 3.4 mmol/100 mL when using 1 atm of CO_2 pressure, faster CH_4 and H_2 productions than when $NaHCO_3$ is used (2.3 mmol/100 mL) are expected. However, as shown in Figure 5d, when am-TiO_2-SiO_2 is used, CH_4 is produced 80 times faster (8.9 µmol $g_{cat}^{-1}h^{-1}$) than P25. This is quite a remarkable result for a solid-liquid condition since this rate is even more significant than when Pt-TiO_2 is used; it is reported at 1.4 and 5.2 $\mu mol g_{cat}^{-1}h^{-1}$ using solid-liquid and solid-gas conditions [44]. For hollow anatase, single crystal and mesocrystal values of 0.2, 1, and 1.7 $\mu mol g_{cat}^{-1}h^{-1}$ have been reported for solid-gas needs [45]. Using carbon-doped amorphous TiO_2, 4.1 $\mu mol g_{cat}^{-1}h^{-1}$ has been reported [32]. A similar rate of 8.9 $\mu mol g_{cat}^{-1}h^{-1}$ has been obtained using 2%MgO-Pt-TiO_2 under solid-gas conditions [44]. This value is one of the best yields reported for

CO_2 photo reduction for non-carbon-based photocatalysts. In the kinetics shown in Figure 5d, pH = 3, CH_4 is produced more significantly than H_2. This is quite an important result since at pH = 8 (Figure 5a and 5b), H_2 is favored instead. This means that acid pH favors CH_4 formation.

In Figure 5d, reuse am-TiO_2-SiO_2 results are also shown. As depicted, the CH_4 rate (3 $\mu molg_{cat}^{-1}h^{-1}$) decreases, and the H_2 rate increases (0.6 $\mu molg_{cat}^{-1}h^{-1}$) compared to catalysts used for the first time at pH = 3. This difference may be due to the difference in pH: 4.6 Vs. 3. As reported in Table 2 at pH = 5, CH_4 rate = 5 $\mu molg_{cat}^{-1}h^{-1}$ and H_2 rate = 0.1 $\mu molg_{cat}^{-1}h^{-1}$. However, catalyst deactivation cannot be discarded since the reused catalyst was obtained via evaporation of water at 90°C for several hours.

To study the H_2/CH_4 selectivity change with pH in more detail, we performed additional experiments in the 5-7 pH range using $NaHCO_3$ and NaH_2PO_4 as buffers. Two critical remarks can be pointed out from Figure S6a's and Figure S6b's results. As observed for pH = 5, without buffer there is more selectivity towards CH_4. It is the maximum rate of CH_4 produced using $NaHCO_3$. A 5 $\mu molg_{cat}^{-1}h^{-1}$ is obtained. A relatively more significant rate than the reported values for other catalysts in solid-liquid or solid-gas conditions [32, 44, 45]. However, this rate is reduced if NaH_2PO_4 buffer is used at the same pH = 5. This means that an inhibition induced by the phosphate buffer occurs. Probably due to the additional consumption of CO_2 via the equilibrium: $CO_2 + H_2O + Na_2HPO_4 = Na_2CO_3 + H_3PO_4$. Therefore, adding phosphate buffer decreases CH_4 and H_2 formation rates, as experimentally observed. However, since H_2 is also formed without CO_2 (Scheme 1), CH_4 formation is more affected than H_2 (Figure S6c and Figure S6d) when buffer is added. These results can be pointed out as experimental evidence for the Scheme 2 mechanism in which H_2 and CH_4 are formed in two paths via partitioning competition of the radical anion formed in the rds. For practical purposes, selectivity CH_4/H_2 can be reversed by adding buffer to the solution and changing pH. Table 2 resumes the H_2 and CH_4 produced ($\mu molg_{cat}^{-1}h^{-1}$) of am-$SiO_2$-$TiO_2$ catalysts under different photo reduction conditions. Water splitting is also shown.

As further evidence for the mechanisms proposed in Scheme 1 and Scheme 3, we measured [CO] and compared its formation rate with [CH_4] and [H_2] ones at pH = 3 (Figure 6). We have also measured product ratios ([CH_4]/[H_2]) with time at two different pHs to obtain the kinetic (t = 0) and thermodynamic main products using ratios extrapolation to t = 0 and the slope of the ratios Vs. Time plots (Figure S7 left and right).

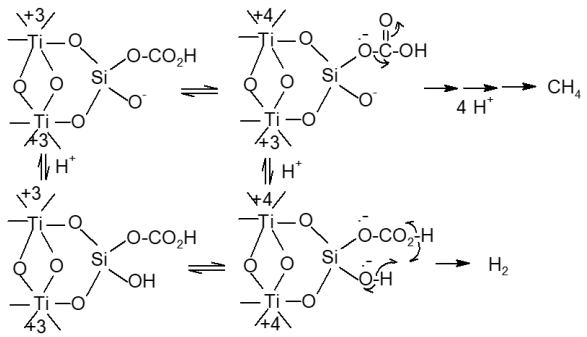

Scheme 3 CH_4 Vs. H_2 formation in the CO_2/HCO_3^- reduction using am-TiO_2-SiO_2. CH_4 rate and selectivity increase by lowering the pH since more protons (4) are required to produce CH_4 than the one needed (2) to yield H_2.

As shown in Figure 6, mainly methane is produced using CO_2 and at pH ca 3. As depicted in the figure inset, some H_2 and CO are also formed in comparable ca. 8 nmol/mL H_2O gcat concentrations after 240 min. From the $[CH_4]/[H_2]$ plot shown in Figure S7 (left), it can be interpreted that both products are formed from the same intermediate that cleaves preferentially to form CH_4 and H_2 (Scheme 3) with some cleavage through the CO path. Although, CH_4 and H_2 are produced from the cleavage of the same intermediate, CH_4 is thermodynamically (t = 240 min, $[CH_4]/[H_2] = 40$) and kinetically (t = 0, $[CH_4]/[H_2] = 28$) more favorable at pH = 3. However, at pH = 8, H_2 is favorably formed. As shown in Figure S7 (right), at t = 0, H_2 and CH_4 are formed in equal concentration, although H_2/CH_4 ratio increases up to 3 after 90 min, probably due to the limited amount of H^+ at this pH. In fact, after 90 min, the ratio slope changes, indicating more than one mechanism for H_2 formation: water splitting (Figure 5c) and Scheme 3. Since in the water splitting mechanism CH_4 is not produced, this mechanism contributes more at the initial $[H_2]/[CH_4]$ reaction times (positive slope, Figure S7 (right)): meanwhile, Scheme 3 one contributes at final reaction times (slightly negative slope, Figure S7 (right)).

3.4 Electrochemical Measurements

Figure 7a shows CVs of P25 and am-TiO_2-SiO_2 coated on ITO. The current intensity is larger for P25 than am-TiO_2-SiO_2, but its de-trapping (positive current) is slower [46]. Less current and slow de-trapping in am-TiO_2-SiO_2 is associated with the catalyst surface capacity to retain a charge. SiO_2 at the surface efficiently includes e; therefore, de-trapping to the solution becomes relatively slow. In the plot of E Vs. t embedded in Figure 7a, an OCPD with smoother decay is observed for am-TiO_2-SiO_2. Figure 7a (embedded) and reported values in Table 3 show that am-TiO_2-SiO_2 halftime is 122 s. Meanwhile, in P25, two slopes are observed with halftimes of 19 s and 103 s. The fast process in P25 corresponds to P25 electron transfer to the electrolyte from its CB and the slow one to electron transfer from oxygen vacancy (Vo) traps. We have reported these two mechanisms, and this OCPD measurement confirms our previous proposal [35]. Another aspect worth mentioning from Figure 7a is the equilibrium potential (surface potential [47]) reached after decay by the two catalysts; as observed in the figure and reported in Table 3, am-TiO_2-SiO_2 reaches a less negative potential than P25. Although the former catalyst´s PZC value (4.1) is relatively lower than the P25 one (6.2), there is more surface negative charge at pH = 7 for P25. This counterintuitive result can be explained in terms of better water solvation in am-TiO_2-SiO_2 compared to P25.

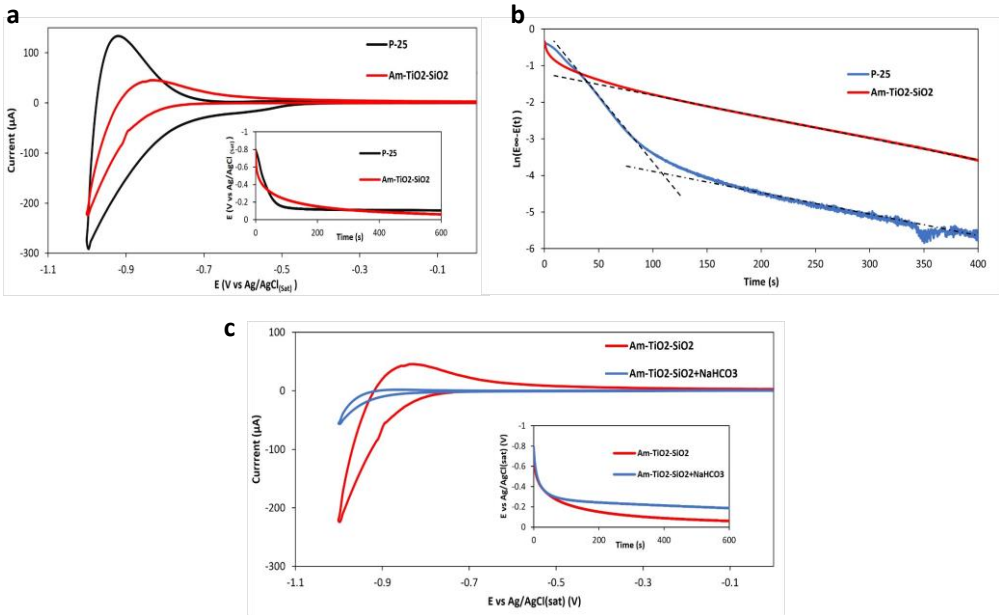

Figure 7 a CV of ITO-P25 and ITO-am-TiO_2-SiO_2. Inset: corresponding open circuit potential decays, after applying a potential of -0.8 V. **b** ln (E_∞-$E_{(t)}$) Vs. time of ITO-P25 and ITO-am-TiO_2-SiO_2. Rates (straight-line slopes) are shown. Values are summarized in Table 3. **c** CV of ITO-am-TiO_2-SiO_2 and ITO-am-TiO_2-SiO_2 adding $NaHCO_3^-$ to the solution. Inset: corresponding open circuit potential decay after applying a potential of -0.8 V.

Table 3 Rate and half-life time values of potential decay ITO-P25, ITO-am-TiO_2-SiO_2, and ITO-am-TiO_2-SiO_2 with $NaHCO_3$ added.

Electrode	1st (150-300) s		2nd (25-75) s		
	rate (s^{-1})	$t_{1/2}$ (s)	rate (s^{-1})	$t_{1/2}$ (s)	Surface Potential[b] (mV Vs Ag/AgCl)
P25	0.0067	103	0.0364	19	-105.4
am-TiO_2-SiO_2	0.0057	122	[a]	[a]	-60.79
am-TiO_2-SiO_2 + $NaHCO_3$	0.0034	204	[a]	[a]	-187.5

[a] Only one slope was detected. [b] A value of -182 mV has been reported for am-TiO_2 [48].

These experiments were performed at pH 7 using NaH_2PO_4 buffer with reduced dissolved O_2 using previously blowing N_2 into the solution; therefore, electron from de-trapping are used to reduce water in the solution. If an additional electron acceptor is added, we expect to observe changes in the corresponding OCPD. As observed in Figure 7c, when $NaHCO_3$ is added to the solution, the capacity of am-TiO_2-SiO_2 to retain charge increases. Also, as shown in Figure 7c, the embedded plot of E Vs. t, the surface charge value obtained is more damaging than the am-TiO_2-SiO_2 and P25 ones (Table 3). This can be interpreted as an additional trap present when $NaHCO_3$ is added. The Adduct shown in Scheme 1 (top right) then acts as a trap that makes more electrons available for photo reduction at the CB. As the figure shows, the destabilization of the two negative charges is diminished since the distance between them in the adduct decreases. This

charge accumulation capability is one of the factors contributing to the efficient methane and hydrogen production when am-TiO_2-SiO_2 is used.

3.5 Photo Reduction Vs. Photo Oxidation

We have used the bleaching induced by OH radical on methylene blue (MB) to test its production by photooxidation of water at the TiO_2 VB [49, 50]. Figure S8a and Table 4 show that quenching effectively occurs when using P25 but does not proceed when am-TiO_2-SiO_2 and P25-TiO_2-SiO_2 are used. We conclude that $OH^{\cdot}$ is not an intermediate in the photooxidation of water. O_2 is then preferentially produced directly or produced from peroxide. The reduction potential for one-electron oxidation to produce hydroxyl radical from water is 2.81 V [51], a higher value than the VB potential of am-TiO_2-SiO_2 (1.93 V) and P25-SiO_2 (2.48 V) [52]. Therefore, one electron transfer is thermodynamically unfavorable; It is only the driven force of the 4 e oxidation to yield O_2 (0.81 V at pH = 7) [52] that allows the first electron transfer to occur, but the product (OH^-) does not accumulate at all. However, the 2 e and 4 e oxidation to produce H_2O_2 and O_2 are feasible since the corresponding potentials at pH = 7 are 1.34 V and 0.81 V, respectively [53]. Conditions for water splitting ($H_2O = H_2 + 1/2O_2$) without a cocatalyst or sacrificial reagent are then provided for am-TiO_2-SiO_2 since the conduction band reduction potential is -1.0 V [53]. Meanwhile, H^+/H_2 at pH 3 and 7 are 0.17 V and -0.41 V, respectively. The non formation of hydroxyl radicals is an excellent advantage for water splitting and CO_2 photoreduction since a sacrificial reagent is unnecessary. Some MB degradation is observed when HCO_3^- is added to the MB solution (Figure S8b and Table 4). Adding HCO_3^- increases the negative charge on its surface, as shown in the surface potential values of Table 3. Increasing the negative charge on the surface induces down-bending on the valence band [54]. Therefore, the VB potential becomes more positive, allowing the one-electron transfer from water to produce a hydroxyl radical that MB quenches. Figure S9 describes the RedOx processes at the am-TiO_2-SiO_2 surface.

Table 4 Methylene Blue (MB) ([MB] = 8 ppm) photooxidation pseudo-first-order rate constants, half times and degradation efficiency after 30 min UV light irradiation. Adding [HCO_3^-] = 4 ppm, last column) significantly improves the activity of less active silicate surface-modified catalysts.

Catalyst 5 mg	pH	k (min^{-1}) Error < 3%	$t_{1/2}$ (min)	% MB photodegradation at t = 30 min	k (min^{-1}) HCO_3^- added Error < 3%
P25	7.2	0.10	6.9	81	[a]
P25-SiO_2	7.2	<0.005	>138	5.6	0.01
am-TiO_2-SiO_2	7.0	<0.005	>138	2.9	0.01

[a] No tested.

The more negative surface charge also favors positively charged organic adsorptions. Efficient MB removal and *E. coli* bacteria inactivation have been reported using P25-SiO_2. In both cases, an effective negative (P25-SiO_2)-positive (MB and protein) interaction is claimed as the leading cause for the improvement in photooxidation rate [55]. The adsorption process is then crucial in these photocatalytic reactions. Likewise, it may play a role in MB's binding inhibition of ACE2

(angiotensin-converting enzyme 2) to SARS-COV$_2$-RBD [56]. The more negative protein the ACE2 active site is, the more efficient MB antiviral activity is predicted.

4. Conclusions

We have prepared silicate-surface modified amorphous TiO_2 (am-TiO_2-SiO_2) and P25 (P25-SiO_2) catalysts. These catalysts yield more CH_4 and H_2 than P25 using UV light. In fact, in 4 h, using 3.4 mmol of CO_2 (1 atm)/100 mL H_2O and 0.3 g of am-TiO_2-SiO_2, 80 times more CH_4 (8.9 $\mu molg_{cat}^{-1}h^{-1}$) than P25 at pH= 3 is produced and 8 times more H_2 (0.84 $\mu molg_{cat}^{-1}h^{-1}$) at pH = 7 when 2.3 mmol of $NaCO_3$/100 mL is used with selectivity's of 71% and 53%, respectively. To our knowledge, 8.9 $\mu molg_{cat}^{-1}h^{-1}$ of CH_4 production in water from CO_2 photo reduction is one of the higher rates reported when using non-carbon-based photocatalysts. H_2 is also formed just by adding water to the am-TiO_2-SiO_2 catalyst. H_2/CH_4 selectivities can be modulated by changing pH and/or using a buffer. H_2 production is favored at neutral pH, and CH_4 at acid pH. Buffer NaH_2PO_4 addition diminishes CH_4 production and barely affects H_2 formation. Due to the low PZC value (4.1) of am-TiO_2-SiO_2 as compared to P25, at pH < 7, faster photo reduction rates are observed since there is a negative charge (-SiO^-) on the surface that promotes CO_2 adsorption, but there is also a proton available (-SiOH) at the active site. Therefore, once the carbonate-catalyst adduct is formed, the electron transfer from Ti to produce the radical anion can be catalyzed by -SiOH. Other factors may also be favoring am-TiO_2-SiO_2 performance as photo-reduction catalyst. Cyclic voltammetry and open circuit potential decay experiments show less intense current and less de-traping for am-TiO_2-SiO_2 than P25, and there is only one smooth decay slope for the former and two slopes for the last catalyst. Therefore, the attached Si at the surface also acts as an external intramolecular trap (EIT) that promotes electron transfer from Ti. When HCO_3^- is added to the solution and the carbonate-catalysts adduct is formed at the surface, a more negative surface potential is measured, meaning that the carbonate at the surface also facilitates the electron transfer from Ti. Additionally, due to the disordered distribution of atoms at the amorphous TiO_2, less e/h recombination occurs. For instance, this catalyst also shows a high light harvesting efficiency with P25-SiO_2. A larger surface area than P25 may also contribute. Meanwhile, CH_4 and H_2 further oxidations at the catalyst interface are avoided in the photo reduction reactions due to the relatively large hydrogen and methane gas-water coefficients, which allow them to accumulate in the reactor headspace.

P25 is a better catalyst than the silicate-modified TiO_2 catalysts for MB photooxidation. The less positive VB potential in the last catalyst makes the OH radical formation from water oxidation unfavorable. Therefore, there is no hydroxyl radical to be quenched by MB. However, when $NaHCO_3$ is added to the solution, these catalyst´s rates increase more than 10 times at neutral pH. The valence band down-bending induced by the more negative surface charge allows some OH radical formation and its corresponding quenching by MB.

The results and mechanism shown in this work have contributed to developing new procedures to increase CO_2 photo-reduction as is the case of coated films at the reactor headspace.

Acknowledgments

This research project is supported by the Second Century Fund (C2F), Chulalongkorn University.

Author Contributions

Oswaldo Núñez: Designing, directing, interpreting and writing manuscript. Mohammad Fereidooni: Synthesis, characterization, photo RedOx experiments and revising manuscript. Victor Márquez: Electrochemical experiments. Duangthip Sattayamuk: Synthesis and characterization. Piyasan Praserthdam: Directing and financing. Supareak Praserthdam: Preliminary calculations and revising manuscript.

Competing Interests

The authors declare no competing financial interest.

Additional Materials

1. Figure S1: Photo reactor setup and CO_2 photo reduction procedure.
2. Figure S2: GC-FID and concentration calculation example.
3. Figure S3: FT IR spectrum, top to bottom of am-P25, am-P25-SiO_2, am-TiO_2 and am-TiO_2-SiO_2. O-Si-O stretching signal at 1022-1080 cm^{-1} is present only in the -SiO_2 catalysts.
4. Figure S4: 80000 x and 200000 x TEM images. Left: am-TiO_2-SiO_2. Right: P25-TiO_2-SiO_2.
5. Figure S5: am-TiO_2 Raman spectrum.
6. Figure S6: a and c Reactor headspace [CH_4] and [H_2] produced in water UV photo reduction of 100 mg of $NaHCO_3$ using 0.3 g of am-TiO_2-SiO_2 at different initial pH (without buffer); b and d Reactor headspace [CH_4] and [H_2] produced in water UV photo reduction of 100 mg of $NaHCO_3$ using 0.3 g of am-TiO_2-SiO_2 using NaH_2PO_4 buffer.
7. Figure S7: Left: [CH_4]/[H_2] ratio Vs. time at pH = 3. Right: [H_2]/[CH_4] ratio Vs. time at pH = 7.4.
8. Figure S8: a 8 ppm of MB photo oxidation using silicate surface-modified TiO_2 catalysts. b ln (C/Co) Vs. time plot of MB UV photo oxidation using P25-SiO_2 and am-TiO_2-SiO_2 catalysts. Pseudo-first order rate constants are found from the corresponding slopes and reported in Table 4.
9. Figure S9: am-TiO_2-SiO_2 RedOx photo-activity. Si acts as an external intramolecular trap (EIT) promoted by the (d-p) π-bonding at the Si-O bond. e/h recombination is then reduced. CH_4 is produced 80 times faster than when P25 is used and H_2 is produced 8 times faster. Only O_2 is produced at the valence band due to its relatively low potential with a value lower than the OH^-/H_2O one. However, when adding HCO_3^- the negative surface charge increases promoting VB down-bending and some OH is produced that is quenched by MB.
10. Table S1: am-TiO_2 Vs. am-TiO_2-SiO_2 BET results.

References

1. Li Y, Li J, Zhang G, Wang K, Wu X. Selective photocatalytic oxidation of low concentration methane over graphitic carbon nitride-decorated tungsten bronze cesium. ACS Sustain Chem Eng. 2019; 7: 4382-4389.
2. Tahir B, Tahir M, Amin NA. Ag-La loaded protonated carbon nitrides nanotubes (pCNNT) with improved charge separation in a monolithic honeycomb photoreactor for enhanced bireforming of methane (BRM) to fuels. Appl Catal B. 2019; 248: 167-183.
3. Xue Q, Wu M, Zeng XC, Jena P. Co-mixing hydrogen and methane may double the energy storage capacity. J Mater Chem A. 2018; 6: 8916-8922.

4. Hayat A, Sohail M, El Jery A, Al Zaydi KM, Raza S, Ali H, et al. Recent advances, properties, fabrication and opportunities in two-dimensional materials for their potential sustainable applications. Energy Storage Mater. 2023; 59: 102780.
5. Hayat A, Sohail M, El Jery A, Al Zaydi KM, Raza S, Ali H, et al. Recent advances in ground-breaking conjugated microporous polymers-based materials, their synthesis, modification and potential applications. Mater Today. 2023; 64: 180-208.
6. Bafaqeer A, Tahir M, Amin NA. Synergistic effects of 2D/2D ZnV_2O_6/RGO nanosheets heterojunction for stable and high performance photo-induced CO_2 reduction to solar fuels. Chem Eng J. 2018; 334: 2142-2153.
7. Bafaqeer A, Tahir M, Ali Khan A, Saidina Amin NA. Indirect Z-scheme assembly of 2D ZnV_2O_6/RGO/g-C_3N_4 nanosheets with RGO/pCN as solid-state electron mediators toward visible-light-enhanced CO_2 reduction. Ind Eng Chem Res. 2019; 58: 8612-8624.
8. Tahir M, Tahir B. 2D/2D/2D O-C_3N_4/Bt/Ti_3C_2Tx heterojunction with novel MXene/clay multi-electron mediator for stimulating photo-induced CO_2 reforming to CO and CH_4. Chem Eng J. 2020; 400: 125868.
9. Tahir B, Tahir M, Nawawi MG. Highly stable 3D/2D WO_3/g-C_3N_4 Z-scheme heterojunction for stimulating photocatalytic CO_2 reduction by H_2O/H_2 to CO and CH_4 under visible light. J CO_2 Util. 2020; 41: 101270.
10. Tahir M. Construction of a stable two-dimensional MAX supported protonated graphitic carbon nitride (pg-C_3N_4)/Ti_3AlC_2/TiO_2 Z-scheme multiheterojunction system for efficient photocatalytic CO_2 reduction through dry reforming of methanol. Energy Fuels. 2020; 34: 3540-3556.
11. Khan AA, Tahir M, Zakaria ZY. Synergistic effect of anatase/rutile TiO_2 with exfoliated Ti_3C_2TR MXene multilayers composite for enhanced CO_2 photoreduction via dry and bi-reforming of methane under UV-visible light. J Environ Chem Eng. 2021; 9: 105244.
12. Tahir M, Tahir B. Constructing S-scheme 2D/0D g-C_3N_4/TiO_2 NPs/MPs heterojunction with 2D-Ti_3AlC_2 MAX cocatalyst for photocatalytic CO_2 reduction to CO/CH_4 in fixed-bed and monolith photoreactors. J Mater Sci Technol. 2022; 106: 195-210.
13. Yu J, Wang K, Xiao W, Cheng B. Photocatalytic reduction of CO_2 into hydrocarbon solar fuels over g-C_3N_4-Pt nanocomposite photocatalysts. Phys Chem Chem Phys. 2014; 16: 11492-11501.
14. Chen X, Wang J, Huang C, Zhang S, Zhang H, Li Z, et al. Barium zirconate: A new photocatalyst for converting CO_2 into hydrocarbons under UV irradiation. Catal Sci Technol. 2015; 5: 1758-1763.
15. Xie K, Umezawa N, Zhang N, Reunchan P, Zhang Y, Ye J. Self-doped $SrTiO_{3-\delta}$ photocatalyst with enhanced activity for artificial photosynthesis under visible light. Energy Environ Sci. 2011; 4: 4211-4219.
16. Yang CC, Yu YH, van der Linden B, Wu JC, Mul G. Artificial photosynthesis over crystalline TiO_2-based catalysts: Fact or fiction? J Am Chem Soc. 2010; 132: 8398-8406.
17. Li P, Zhou Y, Li H, Xu Q, Meng X, Wang X, et al. All-solid-state Z-scheme system arrays of $Fe_2V_4O_{13}$/RGO/CdS for visible light-driving photocatalytic CO_2 reduction into renewable hydrocarbon fuel. Chem Commun. 2015; 51: 800-803.
18. Cybula A, Klein M, Zaleska A. Methane formation over TiO_2-based photocatalysts: Reaction pathways. Appl Catal B. 2015; 164: 433-442.

19. Moustakas NG, Strunk J. Photocatalytic CO_2 reduction on TiO_2-based materials under controlled reaction conditions: Systematic insights from a literature study. Chem Eur J. 2018; 24: 12739-12746.
20. Tahir M. Well-designed $ZnFe_2O_4/Ag/TiO_2$ nanorods heterojunction with Ag as electron mediator for photocatalytic CO_2 reduction to fuels under UV/visible light. J CO_2 Util. 2020; 37: 134-146.
21. Tahir M. Enhanced photocatalytic CO_2 reduction to fuels through bireforming of methane over structured 3D MAX Ti_3AlC_2/TiO_2 heterojunction in a monolith photoreactor. J CO_2 Util. 2020; 38: 99-112.
22. Gao X, Wachs IE. Titania-silica as catalysts: Molecular structural characteristics and physico-chemical properties. Catal Today. 1999; 51: 233-254.
23. Inoue H, Matsuyama T, Liu BJ, Sakata T, Mori H, Yoneyama H. Photocatalytic activities for carbon dioxide reduction of TiO_2 microcrystals prepared in SiO_2 matrices using a sol-gel method. Chem Lett. 1994; 23: 653-656.
24. Anpo M, Chiba K. Photocatalytic reduction of CO_2 on anchored titanium oxide catalysts. J Mol Catal. 1992; 74: 207-212.
25. Yuan L, Han C, Pagliaro M, Xu YJ. Origin of enhancing the photocatalytic performance of TiO_2 for artificial photoreduction of CO_2 through a SiO_2 coating strategy. J Phys Chem C. 2016; 120: 265-273.
26. Zhan S, Yang Y, Gao X, Yu H, Yang S, Zhu D, et al. Rapid degradation of toxic toluene using novel mesoporous SiO_2 doped TiO_2 nanofibers. Catal Today. 2014; 225: 10-17.
27. Kim CS, Shin JW, An SH, Jang HD, Kim TO. Photodegradation of volatile organic compounds using zirconium-doped TiO_2/SiO_2 visible light photocatalysts. Chem Eng J. 2012; 204-206: 40-47.
28. Liu Y, Yu H, Lv Z, Zhan S, Yang J, Peng X, et al. Simulated-sunlight-activated photocatalysis of methylene blue using cerium-doped SiO_2/TiO_2 nanostructured fibers. J Environ Sci. 2012; 24: 1867-1875.
29. Li X, Yu J, Jaroniec M, Chen X. Cocatalysts for selective photoreduction of CO_2 into solar fuels. Chem Rev. 2019; 119: 3962-4179.
30. Sun S, Song P, Cui J, Liang S. Amorphous TiO_2 nanostructures: Synthesis, fundamental properties and photocatalytic applications. Catal Sci Technol. 2019; 9: 4198-4215.
31. Wang P, Yin G, Bi Q, Huang X, Du X, Zhao W, et al. Efficient photocatalytic reduction of CO_2 using carbon-doped amorphous titanium oxide. ChemCatChem. 2018; 10: 3854-3861.
32. Vargas MA, Rodríguez Páez JE. Amorphous TiO_2 nanoparticles: Synthesis and antibacterial capacity. J Non Cryst Solids. 2017; 459: 192-205.
33. Kaur K, Singh CV. Amorphous TiO_2 as a photocatalyst for hydrogen production: A DFT study of structural and electronic properties. Energy Procedia. 2012; 29: 291-299.
34. Calleja G, Serrano DP, Sanz R, Pizarro P. Mesostructured SiO_2-doped TiO_2 with enhanced thermal stability prepared by a soft-templating sol-gel route. Microporous Mesoporous Mater. 2008; 111: 429-440.
35. Núñez O, Sattayamuk D, Saelee T, Yamashita H, Kuwahara Y, Mori K, et al. A closer look inside TiO_2(P25) photocatalytic CO_2/HCO_3^- reduction with water. Methane rate and selectivity enhancements. Chem Eng J. 2021; 409: 128141.

36. Zhu M, Wang H, Keller AA, Wang T, Li F. The effect of humic acid on the aggregation of titanium dioxide nanoparticles under different pH and ionic strengths. Sci Total Environ. 2014; 487: 375-380.
37. Bisquert J, Zaban A, Greenshtein M, Mora Seró I. Determination of rate constants for charge transfer and the distribution of semiconductor and electrolyte electronic energy levels in dye-sensitized solar cells by open-circuit photovoltage decay method. J Am Chem Soc. 2004; 126: 13550-13559.
38. Fabregat Santiago F, Mora Seró I, Garcia Belmonte G, Bisquert J. Cyclic voltammetry studies of nanoporous semiconductors. Capacitive and reactive properties of nanocrystalline TiO_2 electrodes in aqueous electrolyte. J Phys Chem B. 2003; 107: 758-768.
39. Nowacka M, Ambrożewicz D, Jesionowski T. TiO_2-SiO_2/Ph-POSS functional hybrids: Preparation and characterisation. J Nanomater. 2013; 2013: 680821. doi: 10.1155/2013/680821.
40. Song CF, Lü MK, Yang P, Xu D, Yuan DR. Structure and photoluminescence properties of sol-gel TiO_2-SiO_2 films. Thin Solid Films. 2002; 413: 155-159.
41. Gu F, Li CZ, Wang SF, Lü MK. Solution-phase synthesis of spherical zinc sulfide nanostructures. Langmuir. 2006; 22: 1329-1332.
42. Li C, Xiong G, Liu J, Ying P, Xin Q, Feng Z. Identifying framework titanium in TS-1 zeolite by UV resonance Raman spectroscopy. J Phys Chem B. 2001; 105: 2993-2997.
43. Salgado BC, Valentini A. Evaluation of the photocatalytic activity of SiO_2@TiO_2 hybrid spheres in the degradation of methylene blue and hydroxylation of benzene: Kinetic and mechanistic study. Braz J Chem Eng. 2020; 36: 1501-1518.
44. Xie S, Wang Y, Zhang Q, Deng W, Wang Y. MgO-and Pt-promoted TiO_2 as an efficient photocatalyst for the preferential reduction of carbon dioxide in the presence of water. Acs Catal. 2014; 4: 3644-3653.
45. Jiao W, Wang L, Liu G, Lu GQ, Cheng HM. Hollow anatase TiO_2 single crystals and mesocrystals with dominant {101} facets for improved photocatalysis activity and tuned reaction preference. Acs Catal. 2012; 2: 1854-1859.
46. Bertoluzzi L, Badia Bou L, Fabregat Santiago F, Gimenez S, Bisquert J. Interpretation of cyclic voltammetry measurements of thin semiconductor films for solar fuel applications. J Phys Chem Lett. 2013; 4: 1334-1339.
47. Bisquert J, Cendula P, Bertoluzzi L, Gimenez S. Energy diagram of semiconductor/electrolyte junctions. J Phys Chem Lett. 2014; 5: 205-207.
48. Bischoff M, Biriukov D, Předota M, Roke S, Marchioro A. Surface potential and interfacial water order at the amorphous TiO_2 nanoparticle/aqueous interface. J Phys Chem C. 2020; 124: 10961-10974.
49. Satoh AY, Trosko JE, Masten SJ. Methylene blue dye test for rapid qualitative detection of hydroxyl radicals formed in a Fenton's reaction aqueous solution. Environ Sci Technol. 2007; 41: 2881-2887.
50. Nosaka Y, Nosaka A. Understanding hydroxyl radical ($^{\bullet}OH$) generation processes in photocatalysis. ACS Energy Lett. 2016; 1: 356-359.
51. Armstronga DA, Huie RE, Lymar S, Koppenol WH, Merényi G, Neta P, et al. Standard electrode potentials involving radicals in aqueous solution: Inorganic radicals. BioInorg React Mech. 2013; 9: 59-61.

52. Fereidooni M, Núñez O, Márquez V, Paz CV, Villanueva MS, Tun MZ, et al. Effect of substrate conductivity on charge transfer and CO_2 photoreduction in water vapor over silica-modified TiO_2 films. Appl Surf Sci. 2023; 611: 155595.
53. Wood PM. The potential diagram for oxygen at pH 7. Biochem J. 1988; 253: 287-289.
54. Zhang Z, Yates Jr JT. Band bending in semiconductors: Chemical and physical consequences at surfaces and interfaces. Chem Rev. 2012; 112: 5520-5551.
55. Martín Sómer M, Benz D, van Ommen JR, Marugán J. Multitarget evaluation of the photocatalytic activity of P25-SiO_2 prepared by atomic layer deposition. Catalysts. 2020; 10: 450. doi: 10.3390/catl10040450.
56. Bojadzic D, Alcazar O, Buchwald P. Methylene blue inhibits the SARS-CoV-2 spike-ACE2 protein-protein interaction-a mechanism that can contribute to its antiviral activity against COVID-19. Front Pharmacol. 2021; 11. doi: 10.3389/fphar.2020.600372.